A Solar Photothermocatalytic approach for the CO_2 conversion: Investigation of different synergisms on CoO-CuO/Brookite TiO_2-CeO_2 catalysts

Roberto Fiorenza[a,], Marianna Bellardita[b,*], Stefano Andrea Balsamo[a], Luca Spitaleri[a,c], Antonino Gulino[a,c], Marcello Condorelli[a], Luisa D'Urso[a], Salvatore Scirè[a,d] and Leonardo Palmisano[b]*

[a] *Dipartimento di Scienze Chimiche, Università di Catania, Viale A. Doria 6, 95125 Catania, Italy*

[b] *Dipartimento di Ingegneria, Università di Palermo, ed. 6, Viale delle Scienze, 90128 Palermo, Italy*

[c] *I.N.S.T.M., UdR of Catania, Viale A. Doria 6, 95125 Catania, Italy*

[d] *C.I.R.C.C., UdR of Catania, Viale A. Doria 6, 95125 Catania, Italy*

* Corresponding authors: *e-mail address*: rfiorenza@unict.it
marianna.bellardita@unipa.it

Abstract

The photoactive features of the least common polymorph of TiO_2, i.e. brookite, were combined with the thermocatalytic redox ones of cerium oxide, focusing on the effects of the addition of small amounts of Co-Cu oxides for the solar CO_2 conversion. By considering the characterization data, surface segregation of the hosted metal oxides on the TiO_2-CeO_2 composite was evidenced, and their presence increased the amount of oxygen vacancies and improved the charge carriers separation. The bimetallic oxides-based sample was the most performing one in the photocatalytic carbon dioxide reduction at room temperature. The formation of carbon monoxide and methane was 5 and 0.5 μmol/g·h, respectively, i.e. about 10 times higher than that found with bare brookite. A further enhancement was obtained with the same CoO-CuO/TiO_2-CeO_2 catalyst applying the photothermal approach. The CO_2-TPD and the FTIR

measurements highlighted the high interaction between CO_2 and the surface sites.

Keywords: CO_2 valorization, photothermo-catalysis, brookite TiO_2, CeO_2, bimetallic oxides.

1. Introduction

The production of solar fuels, directly obtained through the photocatalytic conversion of carbon dioxide, is a charming route that fits the principles of the green and sustainable chemistry [1]. This process is usually called "artificial photosynthesis" because it allows the formation of value-added fuels (as CO, CH_4, CH_3OH, etc.) starting from CO_2 and merely using a semiconductor photocatalyst irradiated with solar light [2,3]. Among the inorganic semiconductors employed for the photocatalytic reduction of CO_2, titanium dioxide (TiO_2, titania) is one of the most investigated materials, due to its low cost, low toxicity, and high stability [4,5]. However, TiO_2 showed a low activity under the solar light irradiation, due to its wide band-gap (ca. 3.0, 3.2 and 3.3 eV, depending on the crystalline polymorphs, i.e. rutile, anatase, and brookite, respectively). Furthermore, due to the presence of surface acid sites on TiO_2, a weak interaction can occur between titania and CO_2, with a low activation of the latter molecule [5,6]. The addition of co-catalysts with basic surface properties or the preparation of TiO_2-based composites are effective strategies to improve the CO_2 adsorption and its conversion into fuels, providing also an efficient charge carriers separation [7]. To further improve the conversion and the selectivity towards the solar fuels, it is possible to exploit the synergism between photocatalytic and thermocatalytic processes [8,9]. The simultaneous action of heating and solar photoexcitation favours the reduction of CO_2, which is an endothermic reaction and the contemporary water oxidation [10,11].

In this context, the coupling of the photocatalytic features of TiO_2 and the thermocatalytic redox ones of cerium oxide (CeO_2, ceria) can be an efficient approach to increase the photocatalytic activity of TiO_2 [12–14]. Several beneficial effects can derive from the presence of CeO_2 as hosted oxide of TiO_2 in the photo(thermo) reduction of CO_2 because (i) the surface basic sites of cerium oxide can improve the CO_2 adsorption, favouring its activation [15]; (ii) the TiO_2-CeO_2 heterojunction avoids the recombination between the photoproduced electrons and holes [12,16]; (iii) the high mobility of oxygen on the surface of ceria favours the redox cycle Ce^{4+}/Ce^{3+} inducing

the increase of non-stoichiometric cerium oxide species. Indeed, these defective sites can be occupied by the oxygen atoms of CO_2, increasing its adsorption and decreasing its activation energy [17,18].

Taking in account the above considerations, we studied the solar photothermal catalytic reduction of CO_2 in the gaseous phase, using water vapour as a reducing agent and examining the changes in the physico-chemical properties and the (photo)catalytic activity of the TiO_2-CeO_2 composites after the addition of a small amount of CoO-CuO as co-catalysts.

To date, few studies are present in the literature that focus on the exploration of the photo/photothermocatalytic activity of bimetallic oxides supported on TiO_2-based composites and especially brookite TiO_2.

In particular, the research on CO_2 photoreduction has mainly focused on gold-based samples [19,20], while the use of bimetallic oxide systems (based on transition metals) by coupling the photo- and thermo-catalysis has not been sufficiently investigated to the best of our knowledge.

The crystalline phase brookite of TiO_2 has been less studied than rutile and anatase due to the difficulty in obtaining it pure [21]. However, its moderate depth of photoelectron trap [22] combined with the redox properties of CeO_2 can greatly increase the reactivity of photoholes and photoelectrons of composite samples [13].

Finally, the presence of the mixed copper-cobalt oxides can raise the amount of oxygen vacancies of the brookite-ceria composite. Furthermore, the bimetallic species can also act as a system capable of storing/releasing electrons and/or holes [8,23].

In this work, the correlations between the multicatalytic approach (thermocatalysis-photocatalysis) and the various synergisms between brookite TiO_2 and CeO_2 and this composite with the bimetallic oxides, were examined for the CO_2 conversion.

2.1. Catalysts preparation

The thermohydrolysis of $TiCl_4$ in HCl solution was used to synthetize the brookite TiO_2, following the procedure described in the literature [24].

Brookite TiO_2-1wt% CeO_2, TiO_2-3wt% CeO_2 and TiO_2-5wt% CeO_2 were prepared by wetness impregnation on the as-prepared brookite. The cerium(III) nitrate hexahydrate was used as ceria salt precursor. The powders underwent the following thermal

treatments: drying at 120°C and calcination in air at 350°C for four hours. The obtained composites were coded as TiCe1, TiCe3 and TiCe5, respectively, where 1, 3 and 5 indicate the nominal weight percentage of CeO_2.

The Co and Cu species were added by wetness impregnation on TiCe3 to synthesize mono CoO or CuO (0.5wt%) and CoO-CuO bimetallic (0.3wt%-0.3%wt%) oxide catalysts. The precursors were cobalt(II) nitrate hexahydrate and copper(II) nitrate pentahemihydrate. After drying at 120°C the samples were calcined at 300°C for two hours. They were coded as Co/TiCe3, Cu/TiCe3 and Co-Cu/TiCe3.

2.2. Catalysts characterization

The Raman spectra were obtained irradiating the catalysts with a 514.5 nm laser utilizing the instrument and the procedures reported in the ref. [13].

X-ray diffraction patterns of the samples were aquired at room temperature by a PANalytical Empyrean diffractometer equipped with a PIXcel^{1D} (tm) detector using the CuKα radiation and a 2θ scan rate of 1.28 min^{-1}. The UV-Vis DRS (Diffuse Reflectance Spectroscopy) was carried out with the spectrometer Cary 60. The E_g (optical band gap) of the semiconductors was calculated by plotting the modified Kubelka–Munk function vs the hν following the procedure reported in the literature [25].

The photoluminescence properties of the samples were determined using a JobinYvon instrument (Horiba) using an excitation λ of 300 nm.

The BET surface area of the samples was measured using a Thermo Quest (Sorptomatic 1990) apparatus. The powders were outgassed for 24 h at 250°C.

The TEM characterization was made by a Jeol 2100F working at 200 kV. The d_{TEM} (average particle diameter size) was calculated considering the number of particles (n_i) of diameter (d_i) and this correlation: $d_{TEM} = \Sigma(n_i d_i)/n_i$ with around 150 metal oxides particles considered on each sample.

The XPS (X-ray photoelectron spectroscopy) was performed using the Al Kα X-ray with the instrument and the experimental details reported in the ref. [26]. Note that 3% by nominal weight of CeO_2 in TiO_2 corresponds to a real percentage of 1.42 in moles of CeO_2 in TiO_2. In addition, the nominal 0.5% CoO, 0.5% CuO, 0.3% CoO-0.3% CuO values in the TiO_2-CeO_2 composite correspond to 0.14%, 0.17%, 0.08% -0.11%, moles of CoO, CuO, CoO-CuO.

The FTIR spectroscopy was performed with a Spectrum Two System (Perkin Elmer). The background spectrum was recorded with KBr pellet.

The CO_2 TPD (Temperature Programmed Desorption) measurements were performed in a home-made quartz reactor utilizing 150 mg of samples. The CO_2 flow (30 cc/min) was stopped after adsorption and surface saturation processes. Subsequently the reactor was heated from 50°C to 600°C (rate of 10°C/min). After desorption the products were analysed with a mass spectrometer (Sensorlab VG Quadrupoles). The catalysts were pre-treated with a He flow (30 cc/min) for 1 h at 250°C.

2.3. Catalytic activity experiments

The CO_2 photoreduction at room temperature was performed using a home-made quartz reactor, filling it with 0.2 g of catalyst and irradiating with a solar lamp (Osram Ultra Vitalux 300W, irradiance of 10.7 mW/cm^2). The temperature was maintained constant through a fan located near the photoreactor. Before the photocatalytic tests, the samples were left overnight under He flow and UV irradiation (using a 100W mercury lamp, Black-Ray B-100A, 365 nm) in order to desorb the possible impurities and the carbonaceous species arising from the sample surface. Subsequently, water vapour was introduced together with the He under irradiation and various portions of the gas leaving the reactor were analysed by gas-chromatography (GC) to monitor the effectiveness of the cleaning process and the possible presence of residual carbonaceous contamination [27].

Before starting the batch photo- and photothermo-catalytic tests, a mixture of CO_2 and H_2O vapour were flowed in the photoreactor to achieve the saturation of the catalyst surface with the reagent molecules. The water vapour produced from a bubbler maintained at 80°C was mixed with CO_2 (99.999%). By means of a mass flow controller, a CO_2/H_2O mixture with a molar ratio of 15 was obtained. After some preliminary tests, this ratio was chosen because it favoured the CO_2 reduction rather than the competitive water splitting reaction that produced H_2 [28]. For the photothermal catalytic tests the same setup was used heating the reactor at the chosen temperature and irradiating it with the solar lamp.

The reaction products were examined with the Agilent 6890N gas chromatograph (HP-PLOT Q column, TCD detector) calibrated for the detection of methane and carbon

monoxide, and with the Trace GC instrument (Porapak Q column, FID detector) used to detect the possible formation of organic compounds. For the reusability tests, the cleaning steps described above were repeated on the as-used sample before carrying out the subsequent runs.

3. Results

3.1 Structural, textural and morphological properties

One of the critical issues in the use of brookite TiO_2 is the choice of the appropriate preparation method and the thermal treatments to obtain a pure brookite crystalline phase, without rutile and anatase [21]. The thermohydrolysis of $TiCl_4$ in HCl solution is an established procedure to obtain pure brookite [24]. Raman spectroscopy was employed to verify the presence of pure brookite phase and to analyze the structural properties of the as-synthesized composites. Compared to XRD characterization the Raman spectroscopy is more accurate for brookite detection due to the detection of typical vibration modes, whereas to clearly identify the XRD brookite signals, a structure refinement method is required [21] .

The Fig. 1A illustrates the Raman spectra of the samples. The bare brookite TiO_2 showed 10 vibrational modes, assigned on the basis of the literature data to: 4 A_{1g} modes (the main one at 154 cm^{-1} and the others at 249, 417 and 633 cm^{-1}), 2 B_{1g} (213 and 325 cm^{-1}), 2 B_{2g} (367 and 463 cm^{-1}) and 2 B_{3g} (500 and 545 cm^{-1}), whereas the other bands that are present with a very low intensity at 128 cm^{-1}, at 195 cm^{-1} (overlapped with the B_{1g} band at 213 cm^{-1}) and at 586 cm^{-1}, are assigned to other 2 A_{1g} vibrational modes and to another one B_{2g} mode [13,24] respectively.

The typical vibrational mode at 154 cm^{-1} is characteristic of the brookite phase and the absence of vibrational bands at 516 cm^{-1} (due to anatase TiO_2) and 446 cm^{-1} (rutile TiO_2) confirmed the pure brookite formation [13,24], as also verified with the XRD patterns of all the investigated samples (Fig. S1).

In the composites with CeO_2, the main vibrational mode of cerium oxide at 463 cm^{-1} related to the F_{2g} vibrational mode of the cubic fluorite structure [29] overlaps with the second B_{2g} mode of brookite. The absence of signals related to the Cu and/or Co species in the Co/TiCe3, Cu/TiCe3 and Co-Cu/TiCe3 samples, can be due to the low amount of the metal species present in the composites and/or to their good dispersion on the

brookite-ceria composite [30]. The structural modifications related to the metal oxides are indeed highlighted by the Raman shift of the main brookite band (Fig. 1B). In particular, a 0.9 cm^{-1} shift to lower wavenumbers was observed in Co/TiCe3 compared to pure brookite. In the bimetallic oxides sample this redshift is more evident (1.9 cm^{-1}). These changes can be attributed to the structural disorders and defects as oxygen vacancies in the brookite structure generated by the addition of cobalt and copper species, especially when they are simultaneously present [31].

The boundary interaction between the TiO_2 and CeO_2 can be noted from the TEM image of TiCe3 (Fig. 2A), although the similar d-space of the (121) planes of brookite TiO_2 (0.28 nm) and the (111) planes of CeO_2 (0.31 nm) did not permit to clearly discriminate the interface between the two oxides [32].

The particle size distribution of the added metal oxides on the TiCe3 and the TEM images of the Co/TiCe3, Cu/TiCe3 and Co-Cu/TiCe3 samples are illustrated in the Figs. 2B-2D.

The estimated mean particle diameter was 6 nm for the cobalt oxide in the Co/TiCe3 sample (Fig. 2B), 13 nm for the CuO in the Cu/TiCe3 (Fig. 2C) whereas in the Co-Cu/TiCe3 catalysts the CoO and CuO oxides exhibited a similar mean size (10 nm and 9 nm for the cobalt and copper oxides respectively, Fig. 2D). This size variation can be due to the establishment of a mutual interaction between the metal oxides particles when they are contemporary present in the TiO_2-CeO_2 composite, thus influencing their growth and their dispersion [33,34]. However, the possible presence of aggregates of nanooxides on the TiCe3 cannot be excluded.

The presence of the cobalt and copper oxides was further confirmed by the SAED patterns analysis (Fig. S2). The d space values of 0.28 and 0.25 nm correspond to the (110) and (111) planes of CuO and CoO nanoxides, respectively [35,36]. The same d spaces values and similar SAED patterns were found for the Co/TiCe3 and Cu/TiCe3 samples.

The textural features of the samples are reported in the Table 1. The presence of ceria caused a notable decrease in the surface area of brookite from 100 m^2/g to 68 m^2/g and a slight increase in the pore volume and the mean pore diameter. The addition of the metal oxides, instead, did not substantially modify the textural features of the TiCe3 sample. These findings can be ascribed to the inclusion of CeO_2 in the TiO_2 and to the

thermal treatments (calcination in air) carried out to eliminate the nitrates of the metal salt precursors of ceria, copper and cobalt [37].

3.2 Optical properties

The optical properties of the samples were determined with the UV-vis DRS and the photoluminescence (PL) spectroscopies.

Figure 3 illustrates the results of the UV-DRS measurements, plotting the Kubelka-Munk function, vs λ. The spectra of brookite TiO_2 and TiCe3 are similar, with no substantial changes due to the addition of ceria, but those of the other samples show a less significant reflectance in the 200-400 nm wavelength range, probably due to an increased absorption by cobalt and copper species present on their surface. The optical band gap of the catalysts with a single metal (the inset of Fig. 3 shows the graph of Co-Cu/TiCe3 as representative sample) are basically the same as that of brookite, being 3.24 eV for the latter, 3.26 eV for the TiCe3 and Cu/TiCe3 composites, and 3.25 eV for the Co/TiCe3 sample, whereas the addition of the bimetallic oxides led to a slightly higher band gap (3.31 eV), probably due to an interaction between the two metallic species which can influence the absorption.

On the contrary, some interesting optical features were detected investigating the photoluminescence responses of the samples (Fig. 4). The PL spectra of pure brookite present four typical bands. In accordance with the literature data, the band at 390 nm is reasonably attributed to the band-to-band emission of titania and that at 432 nm to the self-trapped excitons present in the crystalline structure of brookite. Moreover, the band at 460 nm is due to the presence of oxygen vacancies, and the PL band at 555 nm is usually related to the excited electrons trapped in the mid-gap levels (i.e. defect centers) [38]. In the composite with CeO_2 it can be noticed the occurrence of a quenching of the PL bands at 390 nm and 430 nm, whilst the band at 460 nm of TiO_2 overlaps with those at about 463 nm attributed to the CeO_2 band to band emission [39]. Notably, the addition of the metal oxide species resulted in a further decrease of the PL bands of TiO_2 and CeO_2. A broad band is visible in the 480-510 nm range for the Co/TiCe3 sample probably due to the formation of oxygen vacancies induced by the cobalt oxide [40]. In fact, the presence of small amounts of metal nanoxides, and in particular of cobalt oxides, facilitated the creation of new oxygen vacancies as intrinsic defects inside

the principal oxide (in this case the TiO_2-CeO_2 system) [41]. Generally, a lower intensity of the PL bands is connected to a decrease of the charge recombination among the photoelectrons and the photoholes. Consequently, the diminution of the band intensity can be associated to an increase of the effectiveness in the charge carriers separation [42]. Therefore, the above results indicate that the addition of copper and/or cobalt species to the TiO_2-CeO_2 composites permitted to decrease the photoelectrons/holes recombination and to increase the number of defects in the composite, as confirmed by the Raman measurements. Cobalt oxide can also act as reservoir of oxygen vacancies.

3.3 Surface properties

The surface electronic structure was studied using XPS. Results for the bare brookite TiO_2 showed sharp titanium spin-orbit bands at 459.2 and 465.0 eV (Fig. 5A). A careful deconvolution of the Ti spectrum profile revealed the presence of an additional spin-orbit component at 457.6 and 462.5 eV due to the presence of some surface Ti^{3+} states, as a result of the presence of oxygen vacancies (Fig. S3A) [13,26].

Fig. 5A shows the XPS of TiCe3, Co/TiCe3, Cu/TiCe3 and Co-Cu/TiCe3 catalysts, in the Ti 2p energy region. Apart from a negligible different band broadening, no relevant binding energy differences were detected, being all of them at 0.3 eV of lower binding energy (BE) with respect to the pure brookite TiO_2. This observation can be justified by taking into account the electronegativity of titanium (1.5) larger than that of cerium (1.1), thus indicating their electronic interaction. Fig. S3B shows the fitted representative high-resolution XP spectrum of the Co-Cu/TiCe3 sample in the Ti 2p binding energy region. The fitting required two Gaussian spin-orbit doublets (Ti $2p_{3/2}$ at 458.9 and 457.0 eV; Ti $2p_{1/2}$ at 464.6 and 462.2 eV). The main doublet is associated with the Ti^{4+} species of the brookite phase [13], while the weak doublet shifted ~2 eV to lower binding energy, and it is due to the presence of the residual surface Ti^{3+} cations after interaction with Ce^{4+} ions [43,44].

The O 1s band of pure brookite is centered at 530.7 eV (Fig. S4A) and shows the presence of some Ti-OH hydroxide species, at 532.6 eV [26]. The high-resolution spectra of the O 1s core levels for TiCe3, Co/TiCe3, Cu/TiCe3 and Co-Cu/TiCe3 catalysts (Fig. S4A), display a O 1s peak at 530.4 eV, comparable to that observed for

the TiO_2, also in this case downshifted of 0.3 eV. Again, a sizeable higher binding energy shoulder accounts for some -OH groups.

The Ce 3d XPS of TiCe3 (Fig. S4B) illustrates the overlap of Ce^{4+} and Ce^{3+} states [43]. The double bands at 883.4 and 902.0 eV is assigned to the Ce(IV) $3d^9 4f^2(O\ 2p^4)$ state. The doublet at 886.6 and 905.2 eV is consistent with the Ce(III) $3d^9 4f^2(O\ 2p^5)$ state. Furthermore, the occurrence of Ce^{4+} is also established by the typical band at 917.7 eV (the fitted spectra are reported in Fig. S4C).

For analogous samples, it has been stated that the occurrence of Ce^{3+} may be due to TiO_2 and CeO_2 electronic interactions that cause some reduction of the Ce^{4+} [43]. Obviously, the presence of some Ti^{3+} cations on the TiO_2 surface is essential for this redox process, and we already evidenced a minor spin-orbit component at 457.0 and 462.2 eV due to the not complete axial coordination of the surface Ti cation in TiO_2 that leads to some surface Ti reduction (vide supra) [44]. Practically, any electronic communication between CeO_2 and TiO_2 is limited to the topmost ionic layers of these nanostructures, confirming the presence of a heterojunction between the TiO_2 and CeO_2 interfaces as verified by the TEM measurements. We already evidenced that the Ti 2p states of all catalysts are at 0.3 eV lower BE with respect to pure brookite, while the BE of the Ce^{4+} 3d states in TiCe3 are 0.4 eV at higher BE with respect to the same levels usually observed in the bare CeO_2 (883.0 eV, Fig. S4D). This further underlines the presence of an electronic coupling between Ti and Ce (both Ce^{4+} and Ce^{3+}) ions. Furthermore, the binding energies of both Ce^{4+} and Ce^{3+} 3d levels in systems containing CoO or/and CuO (Fig. S4B) are 0.2 eV at higher values compared to the same bands detected for TiCe3 (883.4 eV), due to the interactions between the Ce, Co and Cu ions. These strong electronic interactions and the redox process between the Ti and Ce ions favoured the formation of oxygen vacancies in the samples [43-45] as also confirmed by Raman and PL measurements.

Fig. 5B shows the XPS of the Co/TiCe3 and Co-Cu/TiCe3 catalysts in the Co 2p energy region. In both cases, the Co $2p_{3/2,1/2}$ bands are at 781.3 and 797.1 eV (15.8 eV spin-orbit coupling) [46]. It has been previously reported that Co 2p ionization energies are not diagnostic of Co^{2+} and Co^{3+} oxidation states since it appears that any intrinsic shift between tetrahedral Co(II) and octahedral Co(III) is compensated by the site potential difference for the two different types of cations. Nevertheless, shakeup

satellites at a binding energy 6 eV higher than the main spin-orbit components (Fig. 5B) are fingerprint of Co^{2+} species [47].

The XPS spectra of the Cu/TiCe3 and Co-Cu/TiCe3 samples in the Cu 2p zone are reported in the Fig. 5C. In both cases, two well-resolved spin-orbit components centered at 933.9 and 953.8 eV are evident with a 19.9 eV spin-orbit separation, consistently with Cu^{2+} states [48].

Finally, XPS atomic concentration analysis provided the surface composition of all investigated catalysts. Atomic Ce/Ti ratios observed in all samples were close to nominal values whilst surface atomic Co/Ti and Cu/Ti ratios were approximately 24 times larger than nominal values in both mono and bimetallic oxide samples, thus indicating the occurrence of a significant surface segregation of cobalt and/or copper. The above finding highlights the fundamental role that these cations play in the catalytic performance of the studied samples that obviously strongly depends on the catalyst surface composition.

3.4 Photocatalytic and photothermocatalytic activity: Effect of CeO_2 addition

A first catalytic screening was performed by using the three TiCe1, TiCe3 and TiCe5 samples synthesized with a rising loading of CeO_2 deposited on brookite TiO_2. The solar photocatalytic conversion of CO_2 at room temperature on these catalysts is reported in the Fig. 6A. Under the experimental conditions used, only CO and CH_4 were detected as reaction products, whereas the amount of evolved hydrogen, arising from the water splitting reaction, was negligible. Specifically, carbon monoxide was the main product of the CO_2 conversion when brookite TiO_2-based photocatalysts were used together with water vapour as the reducing agent [5,14]. The photoconversion of CO_2 to CO requires two electrons with a more negative potential (i.e. -0.53 V at pH 7 vs. NHE) compared to the photoproduction of methane (-0.24 V), which but requires eight electrons [28].

The TiCe3 sample allowed to obtain higher production rates of CO (0.8 μmol $g^{-1}h^{-1}$) and CH_4 (0.09 μmol $g^{-1}h^{-1}$) than the bare brookite (0.5 μmol $g^{-1}h^{-1}$and 0.05 μmol $g^{-1}h^{-1}$ for the CO and CH_4, respectively). A further increase in the cerium oxide amount showed a detrimental effect (Fig. 6A).

In the photothermocatalytic tests (Fig. 6B, T = 120°C) the activity trends both for the CO and the CH_4 evolution were the same as those obtained in the photocatalytic tests at room temperature, i.e.: TiCe3 > TiCe 1≥ Brookite TiO_2 > TiCe5.

For the best composite (TiCe3) the hybrid catalytic approach allowed to increase of 2.5 times the CO photoproduction (2 μmol $g^{-1}h^{-1}$) and 2.2 times the CH_4 formation (0.2 μmol $g^{-1}h^{-1}$). A lower amount of cerium oxide did not substantially change the photo and photothermal activity of pure brookite, whereas a higher quantity had a negative effect. This can be due to the coverage of the surface sites of TiO_2 caused by the ongoing deposition of cerium oxide [12,16].

On the basis of the above results, cobalt and copper species were added only to the TiCe3 sample and the effects of their presence were investigated.

3.5 Photocatalytic and photothermocatalytic activity: Effect of cobalt, copper and cobalt-copper oxides addition

The addition of cobalt and copper oxides allowed to increase the formation of carbon monoxide and methane both in the photocatalytic and photothermocatalytic tests (Fig. 7). The order of photoactivity at room temperature (Fig. 7A) was Co-Cu/TiCe3 > Cu/TiCe3 > Co/TiCe3 > TiCe3> Brookite TiO_2. Compared to the TiCe3 composite, the addition of the two oxides led to an increase in the formation of CO by about 6 times (5 μmol $g^{-1}h^{-1}$) and of CH_4 by 5.5 times (0.5 μmol $g^{-1}h^{-1}$). Cu/TiCe3 was more active than the Co/TiCe3 sample, which in turn showed slightly higher activity (1 and 0.15 μmol $g^{-1}h^{-1}$ for CO and CH_4, respectively) than the TiCe3 composite.

A further positive effect was verified with the multi catalytic approach (Fig. 7B), as also verified with the bare TiO_2-CeO_2 composites (Fig. 6B). The contemporaneous heating/irradiation of the Co-Cu/TiCe3 sample resulted in the highest production of CO (12 μmol $g^{-1}h^{-1}$) and CH_4 (1.8 μmol $g^{-1}h^{-1}$).

Notably, comparing the performance of bare TiCe3 (2 μmol $g^{-1}h^{-1}$and 0.2 μmol $g^{-1}h^{-1}$ for CO and CH_4, respectively) with that of Co-Cu/TiCe3, it is possible to notice that the increase of the methane production detected with the Co-Cu/TiCe3 sample was higher than the increase of the carbon monoxide evolution. Indeed, the CO production increased by 6 times, i.e. the same enhancement verified in the runs performed without

heating, whereas the increase of methane formation in the photothermal tests was 9 times higher, almost doubling the improvement observed with the photocatalytic tests.

The Cu/TiCe3 sample confirmed its higher activity in the photothermal tests compared to the Co/TiCe3 powders, increasing by about 2 times and by 2.6 times the CO (6 μmol $g^{-1}h^{-1}$) and the CH_4 (0.8 μmol $g^{-1}h^{-1}$) production, respectively. This trend was confirmed also with the Co/TiCe3 catalyst, being the CO/CH_4 improvement 3 times higher comparing the photothermocatalytic and the photocatalytic results.

The beneficial effects of the multi catalytic approach are amplified if the performance of pure brookite is compared with that of the Cu-Co/TiCe3 catalyst in the photocatalytic and photothermocatalytic tests (see Figs. 7A and 7B). The use of this latter catalyst led to improve, in fact, both the CO and CH_4 production of about 10 times in the photocatalytic measurements, and of about 8 times for CO and 20 times for CH_4 in the photothermal tests. The photothermo catalytic results in function of the surface area are summarized in the Table 1.

Furthermore, it is important to highlight that for all of the samples, no formation of solar fuels was detected in the thermocatalytic test carried out at temperatures < 300°C and under dark, in accordance with the literature data [4,5].

3.6 CO_2-TPD and FTIR measurements

The CO_2 is an acid molecule, and it is largely used as probe for the investigation of the basicity of the catalysts surface sites [49]. The first step of the CO_2 photoconversion is its adsorption on the surface of the catalyst. The investigation of the CO_2-TPD profiles of the examined catalysts can be useful to determine the strength of the interaction and the nature of the surface basic sites.

The presence of cerium oxide led to exploit its surface basicity that allowed to improve the adsorption of carbon dioxide, with the formation of different carbonates on the surface of the samples. The CO_2-TPD curves (Fig. 8) recorded between room temperature and 600°C can be divided into three parts indicated as α, β and γ, and associated to weak, medium and strong sites, respectively [50]. The weak basic sites are usually identified with the surface hydroxyl groups on metal oxides which form hydrogen carbonate by interacting weakly with CO_2. The α peaks are characteristic of

the linear adsorptive form of CO_2, the β and the γ ones represent the bridge-bonded adsorptive form.

From the Fig. 8 it is clear as the surface sites of the samples changed on the basis of the specific chemical modifications of brookite TiO_2. The pure TiO_2 showed only weak desorption features in the high-temperature zone. The addition of small amount of cerium oxide (TiCe3 sample) led to an increase in the CO_2 adsorption capacity. In fact, slightly more intense signals related to the moderate (β) and strong basic sites (γ) can be observed. Three desorption peaks are visible in the profile of Co/TiCe3, two more intense at 84°C and at 453°C and a feeble one at 246°C, indicating the prevalent introduction of weak and strong basic sites by cobalt. The presence of copper (Cu/TiCe3), on the other hand, introduced moderate basic sites and improved bridge-type adsorption of CO_2. The CO_2-TPD profile of the Co-Cu/TiCe3 points to a strong interaction between the CO_2 and the surface sites of this catalyst as indicated by the presence of the β and γ peaks. Indeed, this sample showed a peak at 308°C, similarly to the Cu/TiCe3 powder, and two peaks at 108°C and 469°C slightly shifted at higher temperature (stronger CO_2 interaction) compared to those of Co/TiCe3. Furthermore, another signal (at 396°C) was detected. The desorption peaks in the range 380-570°C were related to the decomposition of (bidentate) carbonate species, whereas the features between 180-380°C and between 550-780°C are due to the decomposition of hydrogen carbonates and monodentate carbonates respectively [14,50]. Only for a general comparison, the CO_2-TPD curves of the pure CuO, CoO and of CoO-CuO prepared by chemical precipitation are reported in the supporting information (Fig. S5). It is important to highlight, in fact, that a real comparison is not possible considering that in our work the bimetallic Co-Cu oxides were added as co-catalysts in small amount (0.3wt%-0.3wt%) on brookite TiO_2-CeO_2, using a different preparation method (impregnation) compared to the synthesis of the bare CuO, CoO and of the mixture CoO-CuO (that required a chemical precipitation). Furthermore, the CO_2 interaction was influenced by the presence of both the acid sites of TiO_2 and mainly the basic sites of CeO_2.

Surface enrichment of the metal oxides due to phase segregation was noticed on Co/TiCe3, Cu/TiCe3 and Co-Cu/TiCe3 samples, as indicated by XPS results. This facilitated the CO_2 adsorption especially in the Co-Cu/TiCe3 sample where multiple

metal surface sites allowed to establish a strong interaction with CO_2, which occurs instead with much lower strength in the bare brookite and in the TiCe3 composite.

To further confirm the formation of the carbonate species after the adsorption of CO_2 on the surface of the TiCe3-based catalysts, we have compared the FTIR spectra of the Co/TiCe3, Cu/TiCe3 and Co-Cu/TiCe3 samples before and after the photothermocatalytic tests (Fig. 9).

Before the activity runs all samples exhibited the typical FTIR spectra of TiO_2-based materials with a broad band at around 3500-3400 cm^{-1} and a peak at around 1610-1620 cm^{-1} assigned to the stretching and bending modes of the hydroxyl groups, respectively. These bands can be due to both the residual water molecules and the Ti-OH bonds. The broad band observed in the range 700-600 cm^{-1} is attributed to the Ti-O-Ti vibrations (Figs. 9 and S6) [12]. After the photothermal tests, it is possible to note the formation of new bands in the (hydrogen)carbonate zone (1400-1050 cm). All samples showed a strong band at 1383-1384 cm^{-1}, assigned to the symmetric stretching of carboxylate molecules [51]. Co/TiCe3 showed a spectrum with a small signal at 1114 cm^{-1} of the bridged bidentate carbonates [51]. The Cu/TiCe3 sample exhibited signals at 1187 and 1115 cm^{-1} related to bridged carbonates, while the band at 1068 cm^{-1} is assigned to the ν_{C-O} of monodentate carbonate [51]. In the Co-Cu/TiCe3 catalyst, two small bands at 1215 and 1131 cm^{-1} can be assigned to bridged bidentate carbonates, whereas the feature at about 1036 cm^{-1} to small amounts of hydrogen carbonates [51].

The contemporaneous presence of different surface metal sites (mainly Co, Cu and/or Co-Cu centers due to surface segregation as evidenced by XPS) favoured the formation of both hydrogen carbonates and bridged bidentate carbonates species in the Co-Cu/TiCe3 catalyst, with a beneficial effect in the CO_2 reduction. As reported in the literature, the bidentate binding mode of carbon dioxide, with the formation of bidentate carbonates favours the formation of CO through the bidentate formate species as intermediate and a successive transformation of CO into CH_4 [4,52]. Note that during the catalytic and photocatalytic measurements no formic acid was detected. This acid was instead reported as a common product of the CO_2 photoreduction performed in aqueous (liquid) media [28]. Furthermore, the presence of hydrogen carbonates is beneficial because they can act as holes scavenger and can be also converted into other

bidentate formate species [4,52]. This is one of the key features that can explain the improved performance of this bimetallic oxide-based catalyst with respect to the others.

The formation of the carbonate species after the photothermo catalytic measurements was also confirmed by the comparison of the XPS spectra in C 1s region before and after the test (Fig. S7, Co-Cu/TiCe3 chosen as representative sample). All the spectra show the adventitious carbon peak at 285.0 eV, currently used for calibration [26]. Furthermore, the XP spectrum of the sample measured after the CO_2 photoreduction also exhibits a peak at 289.0 eV ascribed to the carbonate species ($–CO_3^{2-}$), thus confirming their formation during the reaction. This signal is not present in the sample analyzed before the photothermal tests, pointing to the absence of carbon impurities (they were removed during the cleaning steps, see par. 2.3) on the surface of the sample.

4. Discussion

The photo(thermo) catalytic results and the characterization data here reported can be discussed in terms of different synergisms, which are involved in determining the final performance of the investigated samples.

The first exploited synergism is the "energy synergism" between the photocatalytic and the thermocatalytic mechanisms. The multi catalytic approach allowed to increase the solar fuel formation (Fig. 6 and Fig. 7). The heating, as well as to increase the rate of the CO_2 conversion and of the water oxidation [10,11], promoted the oxygens mobility of the reducible oxides as CeO_2, CoO and CuO, and the presence of oxygen vacancies in the CeO_2 (generated by the Ce^{3+} species as confirmed by XPS) was further increased by the simultaneous addition of copper and cobalt species in the Co-Cu/TiCe3 sample (as confirmed by XPS, Raman and PL measurements). These oxygen vacancies sensibly decrease the energy for the adsorption of CO_2. It is indeed reported that carbon dioxide preferentially adsorbs on oxygen defective sites [17,18]. Furthermore, to have an efficient CO_2 reduction, the electron and proton transfers should be synchronous. Considering that the time scale for the electron transfer is picoseconds whereas that of proton transfer is hundreds of microseconds, the rate determining step of the reaction should be the H^+ transfer process [6,8]. In this contest, the contemporaneous presence of solar and thermal energy leads to enhance, as reported in the literature, the proton transfers [53] obtaining beneficial multiple protons/electrons transfers.

We want to highlight that this synergism between thermo and photocatalysis had a positive effect only if the photocatalytic mechanism was simultaneously activated. Indeed, no CO and CH_4 formation was detected in the thermocatalytic tests up to 300°C. Although, in fact, the presence of the oxygen vacancies facilitates the adsorption of CO_2, its further conversion requires multi proton/electron transfers, that can be generated by the photocatalytic mechanism, or higher temperatures (T>300°C) necessary for the carbon dioxide dissociation [4,5,54] as also stated by the CO_2-TPD. A confirmation of the mutual positive effect between the photocatalytic and the thermocatalytic mechanisms was highlighted by the solar photothermal results performed at increasing temperature with the most performing sample (the Co-Cu/TiCe3 catalyst) (Fig. S8). The high temperature promotes the CeO_2 redox properties [12] favouring the CO/CH_4 formation. It is possible to notice that the beneficial synergistic effect led to a linear growth in the evolution of CO and CH_4 up to about 2 times every 60° C of temperature increase.

The CO_2-TPD and the FTIR measurements pointed to a peculiar "surface sites synergism" particularly evident on the bimetallic oxides sample, considering also that the XPS stated the surface segregation of these species on the TiCe3. The strong interaction of CO_2 with the multiple metal surface sites favoured its adsorption and activation. Considering the results obtained which highlighted the greater performance of the Co-Cu/TiCe3 catalyst compared to the other samples, the proposed mechanism of photothermocatalytic conversion of CO_2 is illustrated in Fig. 10.

Under solar irradiation, the photogenerated electrons and holes were efficiently separated due to the heterojunction (detected by TEM) between the brookite TiO_2 and the CeO_2. The conduction and the valence band levels of CeO_2 and brookite TiO_2 allowed the generation of CO and CH_4 and the oxidation of water with the formation of H^+ [14]. Copper and cobalt oxides acted as efficient co-catalysts, which allowed to increase the solar fuel formation and to efficiently separate the charge carriers as confirmed by the PL characterization. In fact, the excited electrons can react with the adsorbed CO_2 while the holes interacting with the CoO-CuO co-catalysts, boost up the oxidation of water and the generation of protons. The surface segregation of these oxides on brookite-cerium oxide enabled the improvement of the interaction with

carbon dioxide molecules also favoring the formation of carbonate species as intermediates, which paved the way for the conversion of CO_2 into CO and CH_4.

The contemporaneous presence of CoO and CuO on the surface of TiCe3 led to a holistic effect ("bimetallic oxide synergism") that permitted to increase the catalytic performance compared to the monometallic counterparts. The strong mutual interaction between the two metal oxides, that influenced their growth and dispersion on the TiCe3 as detected by TEM measurements, allowed to join the beneficial properties of copper and cobalt oxides. In particular, the CuO promoted the CO_2 reduction, being an efficient co-catalyst for the electrons donation [5,23], the cobalt oxide facilitated the formation of oxygen vacancies, as detected by PL spectroscopy, and the holes trap, boosting the oxidation of water and protons formation [8,41]. Although these features could be exploited also in the monometallic CoO and CuO catalysts, the simultaneous addition of both oxides on the surface of TiCe3 synergistically increased the solar fuel formation.

Finally, it is important to highlight that these peculiar synergisms were more effective in the presence of the pure brookite phase. Indeed, in the same experimental conditions, we have compared the performance in the photothermal test at 120°C of Co-Cu/TiCe3 sample with those of two samples prepared with the same synthesis but employing commercial anatase (Sigma Aldrich 637254) and rutile (Sigma Aldrich 224227) TiO_2. The use of rutile led to the lowest CO/CH_4 formation (Fig. S9). As reported, the CB energy level of rutile was not appropriate for the CO_2 reduction into CO, whereas the CB edge of anatase was similar to that of brookite [23]. However, with the anatase TiO_2-based composite the CO and CH_4 production were lower (8 and 0.9 $\mu mol\ g^{-1}h^{-1}$ respectively) compared to the brookite-based sample (12 and 1.84 $\mu mol\ g^{-1}h^{-1}$ for CO and CH_4 respectively). The peculiar preparation mode of the pure brookite, its strong interaction with cerium oxide and its specific physico-chemical properties make this crystalline phase particularly suitable for the photoreduction reactions and for multi catalytic approaches [13,55-57]. The good affinity between brookite TiO_2 and CeO_2 was further highlighted by comparing the photothermal activity of the Co-Cu/TiCe3 with those of Co-Cu/brookite TiO_2 and the Co-Cu/CeO_2 (Fig. S10). Indeed, the CO and the CH_4 formation obtained with the Co-Cu/brookite TiO_2 was about two times and five times lower of the Co-Cu/TiCe3 respectively, whereas the Co-Cu/CeO_2 showed a very

low activity being the CO formation 30 times lower than that observed with Co-Cu/TiCe3, without methane evolution.

The 0.3-0.3 wt% was the optimal amount of the bimetallic oxides sample (Fig. S11), whereas a higher amount led to a detrimental effect, presumably due to excessive coverage of the active sites of TiO_2 [12,16].

The Co-Cu/Ti(brookite)Ce3 also showed a good stability after 3 consecutive runs of photothermocatalytic tests at 120°C (Fig. S12) pointing to as the experimental conditions of this hybrid catalysis or the eventual formation of carbonaceous impurities on the surface of the sample, that however were removed during the cleaning steps (par. 2.3), did not affect the catalytic activity of the best performing sample examined in this work.

5. Conclusions

The solar photothermocatalytic conversion of the carbon dioxide was investigated on brookite TiO_2-CeO_2-based catalysts. The influence of the addition of small amounts of cobalt oxide, copper oxide and of the CoO-CuO bimetallic oxides was investigated. For both photocatalytic and photothermocatalytic tests, the CoO-CuO supported on the TiO_2-3% CeO_2 gave the best results. The "multi" properties of this peculiar material and the multi catalytic approach allowed to sensibly increase the CO/CH_4 formation. In particular, the use of Co-Cu/TiCe3 material allowed to exploit: (i) the energy synergism between the catalytic and the photocatalytic mechanisms that increased the CO_2 conversion and favoured efficient e^-/H^+ transfers; (ii) the surface sites synergism that facilitated the CO_2 adsorption and its activation through the formation of carbonates as intermediates; (iii) the bimetallic oxides synergism that promoted an efficient charge carriers separation, the increase of oxygen vacancies on the brookite TiO_2-CeO_2 composite and the surface segregation of the added oxides which boosted the CO_2 conversion and the oxidation of water.

The application of this hybrid catalysis using versatile catalysts possessing both photocatalytic and thermocatalytic properties can be a fascinating strategy to exploit CO_2 through solar fuel production.

Acknowledgments

The PON AIM project of the European Social Found (for the author R.F.) and the PIACERI 2020-2022 project of the University of Catania (for the authors S.S., L.D., A.G.) are acknowledged for funding.

References

[1] V.-H. Nguyen, B.-S. Nguyen, Z. Jin, M. Shokouhimehr, H.W. Jang, C. Hu, P. Singh, P. Raizada, W. Peng, S. Shiung Lam, C. Xia, C.C. Nguyen, S.Y. Kim, Q. Van Le, Towards artificial photosynthesis: Sustainable hydrogen utilization for photocatalytic reduction of CO_2 to high-value renewable fuels, Chem. Eng. J. 402 (2020) 126184.

[2] C. Karthikeyan, P. Arunachalam, K. Ramachandran, A.M. Al-Mayouf, S. Karuppuchamy, Recent advances in semiconductor metal oxides with enhanced methods for solar photocatalytic applications, J. Alloys Compd. 828 (2020) 154281.

[3] M. Takht Ravanchi, S. Sahebdelfar, Catalytic conversions of CO_2 to help mitigate climate change: Recent process developments, Process Saf. Environ. Prot. 145 (2021) 172–194.

[4] N.N. Vu, S. Kaliaguine, T.O. Do, Critical Aspects and Recent Advances in Structural Engineering of Photocatalysts for Sunlight-Driven Photocatalytic Reduction of CO_2 into Fuels, Adv. Funct. Mater. 29 (2019) 1–44.

[5] S. Al Jitan, G. Palmisano, C. Garlisi, Synthesis and surface modification of TiO_2-based photocatalysts for the conversion of CO_2, Catalysts. 10 (2020) 227.

[6] K. Li, X. An, K.H. Park, M. Khraisheh, J. Tang, A critical review of CO_2 photoconversion: Catalysts and reactors, Catal. Today. 224 (2014) 3–12.

[7] M. Khalil, J. Gunlazuardi, T.A. Ivandini, A. Umar, Photocatalytic conversion of CO_2 using earth-abundant catalysts: A review on mechanism and catalytic performance, Renew. Sustain. Energy Rev. 113 (2019) 109246.

[8] Y. Li, C. Wang, M. Song, D. Li, X. Zhang, Y. Liu, TiO_{2-x}/CoO_x photocatalyst sparkles in photothermocatalytic reduction of CO_2 with H_2O steam, Appl. Catal. B Environ. 243 (2019) 760–770.

[9] C. Wang, S. Fang, S. Xie, Y. Zheng, Y.H. Hu, Thermo-photo catalytic CO_2 hydrogenation over Ru/TiO_2, J. Mater. Chem. A. 8 (2020) 7390–7394.

[10] S. Roy, A. Cherevotan, S.C. Peter, Thermochemical CO_2 Hydrogenation to Single Carbon Products: Scientific and Technological Challenges, ACS Energy Lett. 3 (2018) 1938–1966.

[11] M.N. Ha, G. Lu, Z. Liu, L. Wang, Z. Zhao, 3DOM-$LaSrCoFeO_{6-\delta}$ as a highly active catalyst for the thermal and photothermal reduction of CO_2 with H_2O to CH_4, J. Mater. Chem. A. 4 (2016) 13155–13165.

[12] R. Fiorenza, M. Bellardita, L. Palmisano, S. Scirè, A comparison between photocatalytic and catalytic oxidation of 2-Propanol over Au/TiO_2-CeO_2 catalysts, J. Mol. Catal. A Chem. 415 (2016) 56–64.

[13] M. Bellardita, R. Fiorenza, L. D'Urso, L. Spitaleri, A. Gulino, G. Compagnini, S. Scirè, L. Palmisano, Exploring the Photothermo-Catalytic Performance of Brookite TiO_2-CeO_2 Composites, Catalysts. 10 (2020) 765.

[14] J. Zhao, Y. Wang, Y. Li, X. Yue, C. Wang, Phase-dependent enhancement for CO_2 photocatalytic reduction over CeO_2/TiO_2 catalysts, Catal. Sci. Technol. 6 (2016) 7967–7975.

[15] Y. Wang, J. Zhao, T. Wang, Y. Li, X. Li, J. Yin, C. Wang, CO_2 photoreduction with H_2O vapor on highly dispersed CeO_2/TiO_2 catalysts: Surface species and their reactivity, J. Catal. 337 (2016) 293–302.

[16] R. Fiorenza, M. Bellardita, T. Barakat, S. Scirè, L. Palmisano, Visible light photocatalytic activity of macro-mesoporous TiO_2-CeO_2 inverse opals, J. Photochem. Photobiol. A Chem. 352 (2018) 25–34.

[17] Y. Ji, Y. Luo, New Mechanism for Photocatalytic Reduction of CO_2 on the Anatase TiO_2 (101) Surface: The Essential Role of Oxygen Vacancy, J. Am. Chem. Soc. 138 (2016) 15896–15902.

[18] L. Yuan, Y.-J. Xu, Photocatalytic conversion of CO_2 into value-added and renewable fuels, Appl. Surf. Sci. 342 (2015) 154–167.

[19] M. Tahir, B. Tahir, N.A.S. Amin, Synergistic effect in plasmonic Au/Ag alloy NPs co-coated TiO_2 NWs toward visible-light enhanced CO_2 photoreduction to fuels, Appl. Catal. B Environ. 204 (2017) 548–560.

[20] X. Cai, J. Wang, R. Wang, A. Wang, S. Zhong, J. Chen, S. Bai, Interface engineering on Janus Pd–Au heterojunction co-catalysts for selective photocatalytic reduction of CO_2 to CH_4, J. Mater. Chem. A. 7 (2019) 5266–5276.

[21] A. Di Paola, M. Bellardita, L. Palmisano, Brookite, the Least Known TiO_2 Photocatalyst, Catalysts. 3 (2013) 36–73.

[22] A. Yamakata, J.J.M. Vequizo, Curious behaviors of photogenerated electrons and holes at the defects on anatase, rutile, and brookite TiO_2 powders: A review, J. Photochem. Photobiol. C Photochem. Rev. 40 (2019) 234–243.

[23] M. Bellardita, A. Di Paola, E. García-López, V. Loddo, G. Marcì, L. Palmisano, Photocatalytic CO_2 Reduction in Gas-Solid Regime in the Presence of Bare, SiO_2 Supported or Cu-Loaded TiO_2 Samples, Curr. Org. Chem. 17 (2013) 2440–2448.

[24] M. Bellardita, A. Di Paola, B. Megna, L. Palmisano, Absolute crystallinity and photocatalytic activity of brookite TiO_2 samples, Appl. Catal. B Environ. 201 (2017) 150–158.

[25] P. Makuła, M. Pacia, W. Macyk, How To Correctly Determine the Band Gap Energy of Modified Semiconductor Photocatalysts Based on UV–Vis Spectra, J. Phys. Chem. Lett. 9 (2018) 6814–6817.

[26] A. Gulino, Structural and electronic characterization of self-assembled molecular nanoarchitectures by X-ray photoelectron spectroscopy, Anal. Bioanal. Chem. 405 (2013) 1479–1495.

[27] M. Dilla, R. Schlögl, J. Strunk, Photocatalytic CO_2 Reduction Under Continuous Flow High-Purity Conditions: Quantitative Evaluation of CH_4 Formation in the Steady-State, ChemCatChem. 9 (2017) 696–704.

[28] E. Karamian, S. Sharifnia, On the general mechanism of photocatalytic reduction of CO_2, J. CO_2 Util. 16 (2016) 194–203.

[29] R.C. de Oliveira, R.A.C. Amoresi, N.L. Marana, M.A. Zaghete, M. Ponce, A.J. Chiquito, J.R. Sambrano, E. Longo, A.Z. Simões, Influence of Synthesis Time on the Morphology and Properties of CeO_2 Nanoparticles: An Experimental–Theoretical Study, Cryst. Growth Des. 20 (2020) 5031–5042.

[30] Z.M. Shammi, A.H. Kianfar, M.M. Momeni, Hydrothermal synthesis and characterization of CuO–CoO/TiO_2 for photocatalytic degradation of methylene blue under visible light and catalytic reduction of P-nitrophenol, J. Mater. Sci. Mater. Electron. 31 (2020) 14810–14822.

[31] V.R. Akshay, B. Arun, G. Mandal, G.R. Mutta, A. Chanda, M. Vasundhara, Observation of Optical Band-Gap Narrowing and Enhanced Magnetic Moment in

Co-Doped Sol–Gel-Derived Anatase TiO_2 Nanocrystals, J. Phys. Chem. C. 122 (2018) 26592–26604.

[32] M. Zeng, Y. Li, M. Mao, J. Bai, L. Ren, X. Zhao, Synergetic Effect between Photocatalysis on TiO_2 and Thermocatalysis on CeO_2 for Gas-Phase Oxidation of Benzene on TiO_2/CeO_2 Nanocomposites, ACS Catal. 5 (2015) 3278–3286.

[33] C. Dai, A. Zhang, L. Luo, X. Zhang, M. Liu, J. Wang, X. Guo, C. Song, Hollow zeolite-encapsulated Fe-Cu bimetallic catalysts for phenol degradation, Catal. Today. 297 (2017) 335–343.

[34] A.E. Aksoylu, M.M.A. Freitas, J.L. Figueiredo, Bimetallic Pt–Sn catalysts supported on activated carbon, Appl. Catal. A Gen. 192 (2000) 29–42.

[35] S.M. Park, A. Razzaq, Y.H. Park, S. Sorcar, Y. Park, C.A. Grimes, S. Il In, Hybrid Cu_xO-TiO_2 Heterostructured Composites for Photocatalytic CO_2 Reduction into Methane Using Solar Irradiation: Sunlight into Fuel, ACS Omega. 1 (2016) 868–875.

[36] X. Zou, Y. Dong, J. Ke, H. Ge, D. Chen, H. Sun, Y. Cui, Cobalt monoxide/tungsten trioxide p-n heterojunction boosting charge separation for efficient visible-light-driven gaseous toluene degradation, Chem. Eng. J. 400 (2020) 125919.

[37] B. Małecka, A. Łącz, E. Drozdz, A. Małecki, Thermal decomposition of d-metal nitrates supported on alumina, J. Therm. Anal. Calorim. 119 (2015) 1053–1061.

[38] X. Shen, B. Tian, J. Zhang, Tailored preparation of titania with controllable phases of anatase and brookite by an alkalescent hydrothermal route, Catal. Today. 201 (2013) 151–158.

[39] S. Phoka, P. Laokul, E. Swatsitang, V. Promarak, S. Seraphin, S. Maensiri, Synthesis, structural and optical properties of CeO_2 nanoparticles synthesized by a simple polyvinyl pyrrolidone (PVP) solution route, Mater. Chem. Phys. 115 (2009) 423–428.

[40] J. Lim, Y. Yang, M.R. Hoffmann, Activation of Peroxymonosulfate by Oxygen Vacancies-Enriched Cobalt-Doped Black TiO_2 Nanotubes for the Removal of Organic Pollutants, Environ. Sci. Technol. 53 (2019) 6972–6980.

[41] A.C. Pradhan, T. Uyar, Morphological Control of Mesoporosity and Nanoparticles within Co_3O_4-CuO Electrospun Nanofibers: Quantum

Confinement and Visible Light Photocatalysis Performance, ACS Appl. Mater. Interfaces. 9 (2017) 35757–35774.

[42] B. Choudhury, P. Chetri, A. Choudhury, Oxygen defects and formation of Ce^{3+} affecting the photocatalytic performance of CeO_2 nanoparticles, RSC Adv. 4 (2014) 4663–4671.

[43] S. Watanabe, X. Ma, C. Song, Characterization of Structural and Surface Properties of Nanocrystalline TiO_2−CeO_2 Mixed Oxides by XRD, XPS, TPR, and TPD, J. Phys. Chem. C. 113 (2009) 14249–14257.

[44] B. Bharti, S. Kumar, H.-N. Lee, R. Kumar, Formation of oxygen vacancies and Ti^{3+} state in TiO_2 thin film and enhanced optical properties by air plasma treatment, Sci. Rep. 6 (2016) 32355.

[45] S. Yuán, B. Xu, Q. Zhang, S. Liu, J. Xie, M. Zhang, T. Ohno, Development of the Visible- Light Response of CeO_{2-x} with a high Ce^{3+} Content and Its Photocatalytic Properties, ChemCatChem. 10 (2018) 1267–1271.

[46] V.A. de la Peña O'Shea, M. Consuelo Álvarez Galván, A.E. Platero Prats, J.M. Campos-Martin, J.L.G. Fierro, Direct evidence of the SMSI decoration effect: the case of Co/TiO_2 catalyst, Chem. Commun. 47 (2011) 7131.

[47] F. Lupo, R. Kamalakaran, A. Gulino, Viable Route for Cobalt Oxide−Carbon Nanocomposites, J. Phys. Chem. C. 113 (2009) 15533–15537.

[48] F. Lupo, S. Gentile, F.P. Ballistreri, G.A. Tomaselli, M.E. Fragalà, A. Gulino, Viable route for switching of an engineered silica surface using Cu^{2+} ions at sub-ppm levels, Analyst. 135 (2010) 2273.

[49] C. Sun, P. Beaunier, P. Da Costa, Effect of ceria promotion on the catalytic performance of Ni/SBA-16 catalysts for CO_2 methanation, Catal. Sci. Technol. 10 (2020) 6330-6341.

[50] Y. Bao, C. Huang, L. Chen, Y. dong Zhang, L. Liang, J. Wen, M. Fu, J. Wu, D. Ye, Highly efficient Cu/anatase TiO_2 {001}-nanosheets catalysts for methanol synthesis from CO_2, J. Energy Chem. 27 (2018) 381–388.

[51] A. Davydov Molecular Spectroscopy of Oxide Catalyst Surfaces, John Wiley &Sons, Inc.: Hoboken, NJ. 2003.

[52] N.M. Dimitrijevic, B.K. Vijayan, O.G. Poluektov, T. Rajh, K.A. Gray, H. He, P. Zapol, Role of water and carbonates in photocatalytic transformation of CO_2 to

CH_4 on titania, J. Am. Chem. Soc. 133 (2011) 3964–3971.

[53] Y. Li, D. Hui, Y. Sun, Y. Wang, Z. Wu, C. Wang, J. Zhao, Boosting thermo-photocatalytic CO_2 conversion activity by using photosynthesis-inspired electron-proton-transfer mediators, Nat. Commun. 12 (2021) 123.

[54] S. Ali, M.C. Flores, A. Razzaq, S. Sorcar, C.B. Hiragond, H.R. Kim, Y.H. Park, Y. Hwang, H.S. Kim, H. Kim, E.H. Gong, J. Lee, D. Kim, S. Il In, Gas phase photocatalytic CO_2 reduction, "a brief overview for benchmarking," Catalysts 9 (2019) 727.

[55] E. Wierzbicka, M. Altomare, M. Wu, N. Liu, T. Yokosawa, D. Fehn, S. Qin, K. Meyer, T. Unruh, E. Spiecker, L. Palmisano, M. Bellardita, J. Will, P. Schmuki, Reduced grey brookite for noble metal free photocatalytic H_2 evolution, J. Mater. Chem. A. 9 (2021) 1168–1179.

[56] L. Liu, Y. Li, Understanding the reaction mechanism of photocatalytic reduction of CO_2 with H_2O on TiO_2-based photocatalysts: A review, Aerosol Air Qual. Res. 14 (2014) 453–469.

[57] M. Cargnello, T. Montini, S.Y. Smolin, J.B. Priebe, J.J.D. Jaén, V.V.T. Doan-Nguyen, I.S. McKay, J.A. Schwalbe, M.M. Pohl, T.R. Gordon, Y. Lu, J.B. Baxter, A. Brückner, P. Fornasiero, C.B. Murray, Engineering titania nanostructure to tune and improve its photocatalytic activity, Proc. Natl. Acad. Sci. U. S. A. 113 (2016) 3966–3971.

Table 1 Textural properties (surface area, mean pore diameter and pore volume) and photothermo catalytic performance (T= 120°C) of the used photocatalysts.

Samples	S_{BET} (m^2/g)	D_m (nm)	V_p (cm^3/g)	CO evolution ($\mu mol/m^2 \cdot h$)	CH_4 evolution ($\mu mol/m^2 \cdot h$)
Brookite TiO_2	100	23.1	0.22	0.03	0.002
TiCe3	68	25.2	0.34	0.06	0.006
Co/TiCe3	69	24.9	0.33	0.09	0.01
Cu/TiCe3	67	25.3	0.33	0.18	0.02
Co-Cu/TiCe3	70	24.7	0.31	0.34	0.05

Captions to figures

Fig. 1 (A) Raman spectra of the analysed catalysts, (B) Zoom of the region of the A_{1g} vibrational mode brookite TiO_2.

Fig. 2 TEM images of TiCe3 (A). Particle size distribution and TEM images of Co/TiCe3 (B), Cu/TiCe3 (C) and Co-Cu/TiCe3 (D).

Fig. 3 Reflectance spectra of the analysed samples. In the inset the band gap determination of the Co-Cu/TiCe3 as representative catalyst.

Fig. 4 Photoluminescence spectra of the analysed samples ($\lambda_{excitation}$ = 300 nm).

Fig. 5 (A) XPS spectra of the examined samples in the Ti 2p binding energy zone; (B) XPS spectra of Co/TiCe3 and Co-Cu/TiCe3 samples, in the Co 2p zone; (C) Cu/TiCe3 and Co-Cu/TiCe3 samples, in the Cu 2p zone.

Fig. 6 (A) Solar photocatalytic CO_2 reduction at room temperature, (B) Photothermocatalytic tests at t =120°C on the brookite TiO_2-CeO_2 composites. The catalysts were irradiated for 5 h.

Fig. 7 (A) Solar photocatalytic CO_2 reduction at room temperature, (B) Photothermocatalytic tests at t =120°C on the TiCe3-based samples. The catalysts were irradiated for 5 h.

Fig. 8 CO_2-TPD curves of the analysed catalysts in the 50-600°C temperature range The α, β, and γ zones identify the weak, medium and strong basic sites, respectively.

Fig. 9 FTIR spectra before and after the photothermocatalytic CO_2 reduction on Co/TiCe3, Cu/TiCe3 and Co-Cu/TiCe3.

Fig. 10 Proposed photothermocatalytic mechanism with the Co-Cu/TiCe3 catalyst.

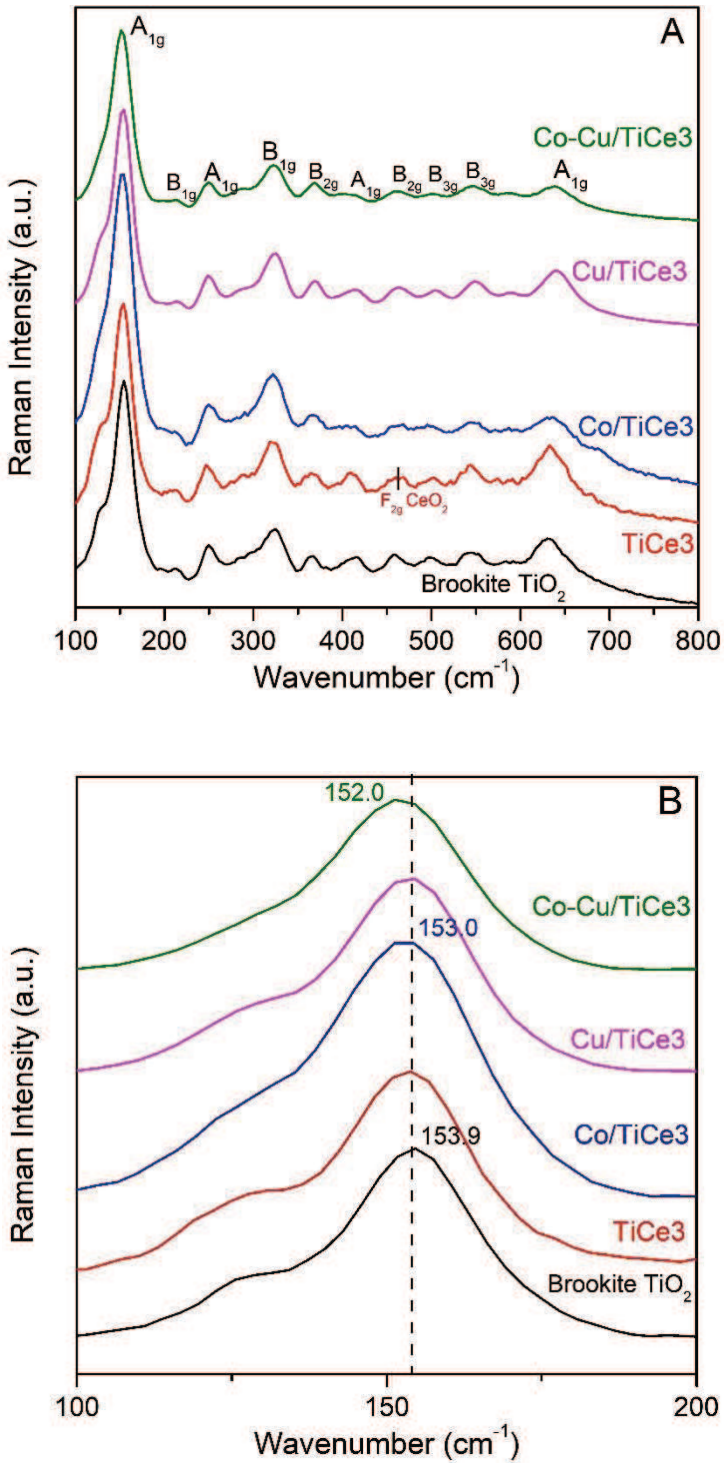
A
A1g
B1g
A1g
B1g
B2g
A1g
B2g
B3g
B3g
A1g
Co-Cu/TiCe3
Cu/TiCe3
Co/TiCe3
F2g CeO2
TiCe3
Brookite TiO2
Raman Intensity (a.u.)
100
200
300
400
500
600
700
800
Wavenumber (cm-1)
B
152.0
Co-Cu/TiCe3
153.0
Cu/TiCe3
Co/TiCe3
153.9
TiCe3
Brookite TiO2
Raman Intensity (a.u.)
100
150
200
Wavenumber (cm-1)

Fig. 1

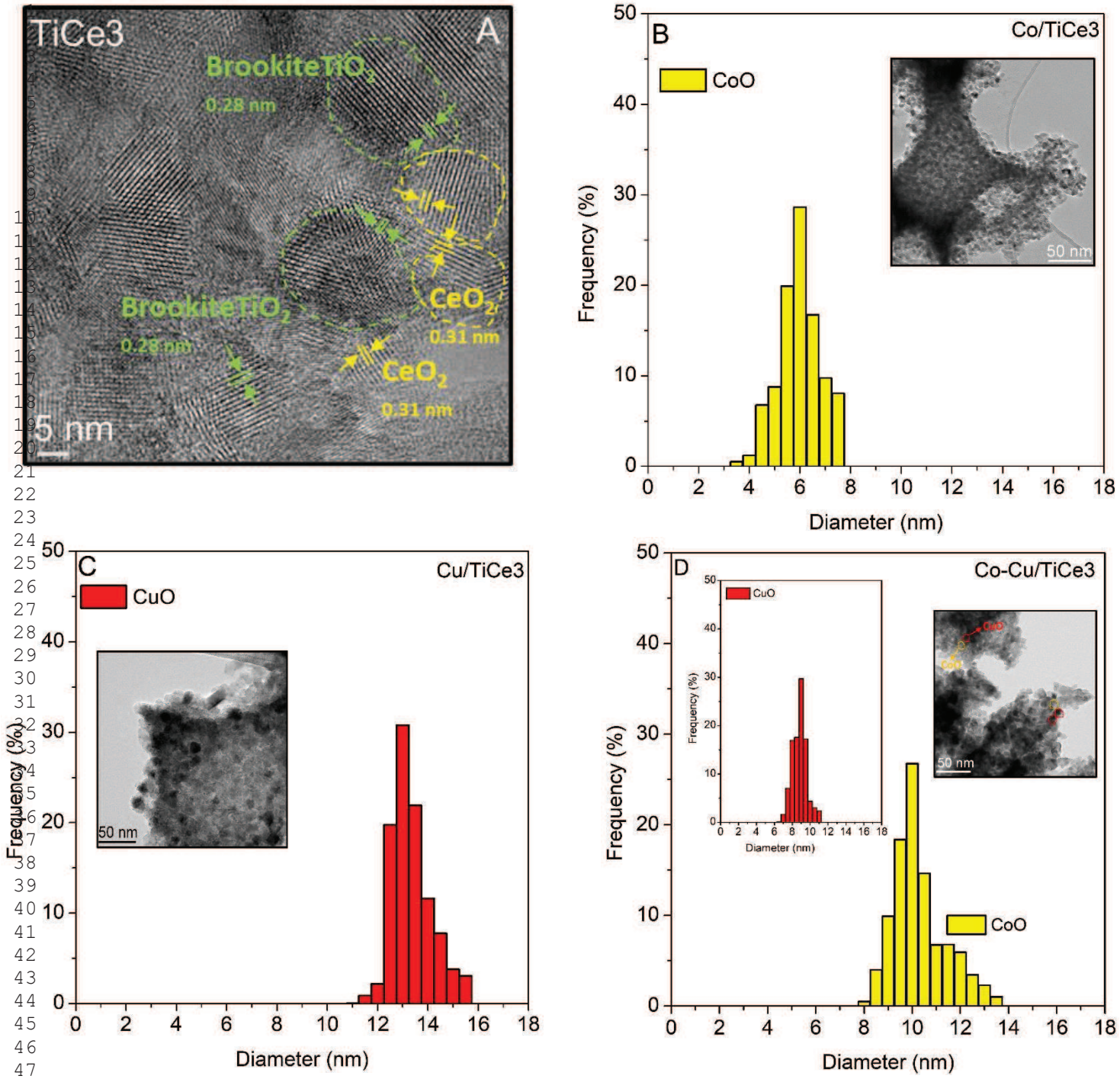
TiCe3
A
Brookite TiO2
0.28 nm
Brookite TiO2
0.28 nm
CeO2
0.31 nm
CeO2
0.31 nm
5 nm
B
Co/TiCe3
CoO
Frequency (%)
Diameter (nm)
50 nm
C
Cu/TiCe3
CuO
Frequency (%)
Diameter (nm)
50 nm
D
Co-Cu/TiCe3
CuO
CoO
Frequency (%)
Diameter (nm)
50 nm

Fig. 2

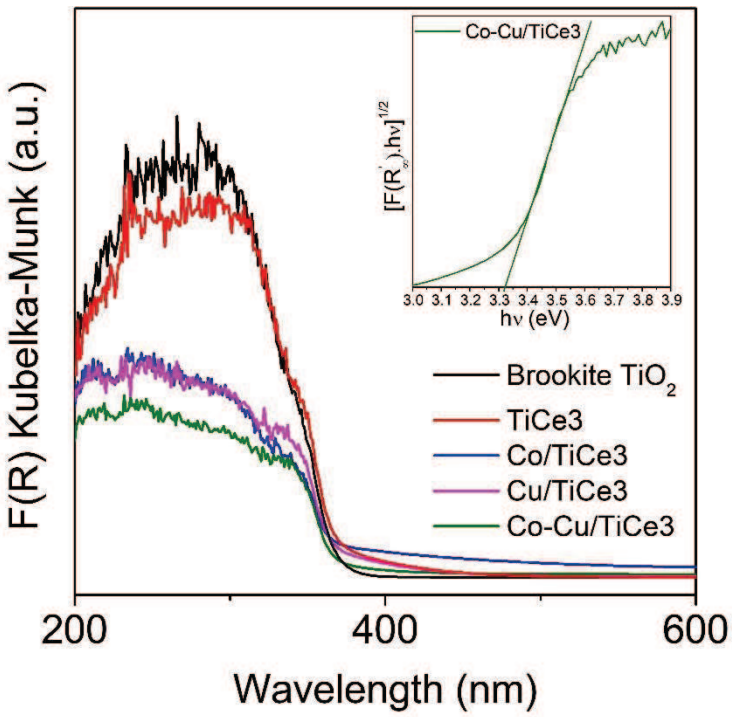
F(R) Kubelka-Munk (a.u.)
Wavelength (nm)
200
400
600
Co-Cu/TiCe3
[F(R∞).hν]^1/2
hν (eV)
3.0 3.1 3.2 3.3 3.4 3.5 3.6 3.7 3.8 3.9
Brookite TiO2
TiCe3
Co/TiCe3
Cu/TiCe3
Co-Cu/TiCe3

Fig. 3

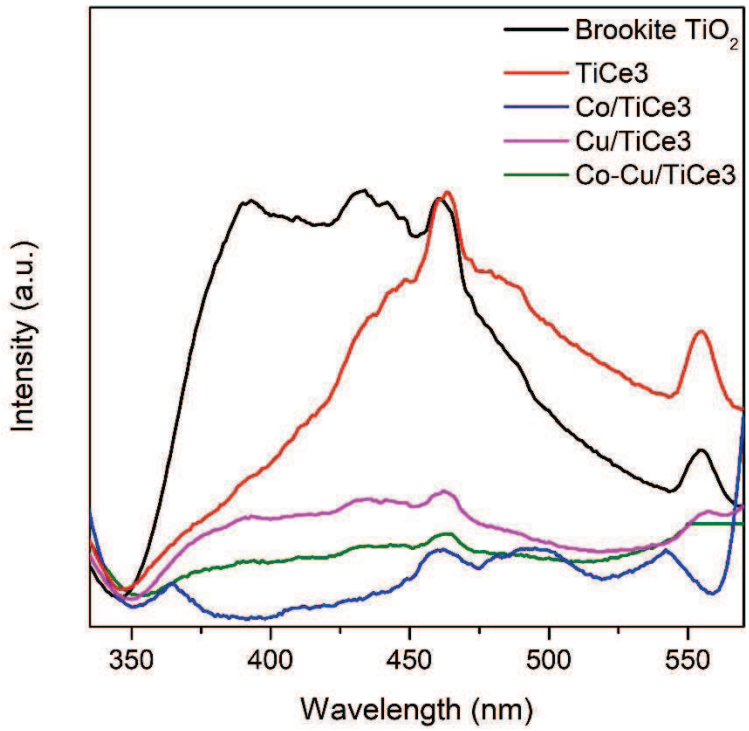
Brookite TiO2
TiCe3
Co/TiCe3
Cu/TiCe3
Co-Cu/TiCe3
Intensity (a.u.)
350
400
450
500
550
Wavelength (nm)

Fig. 4

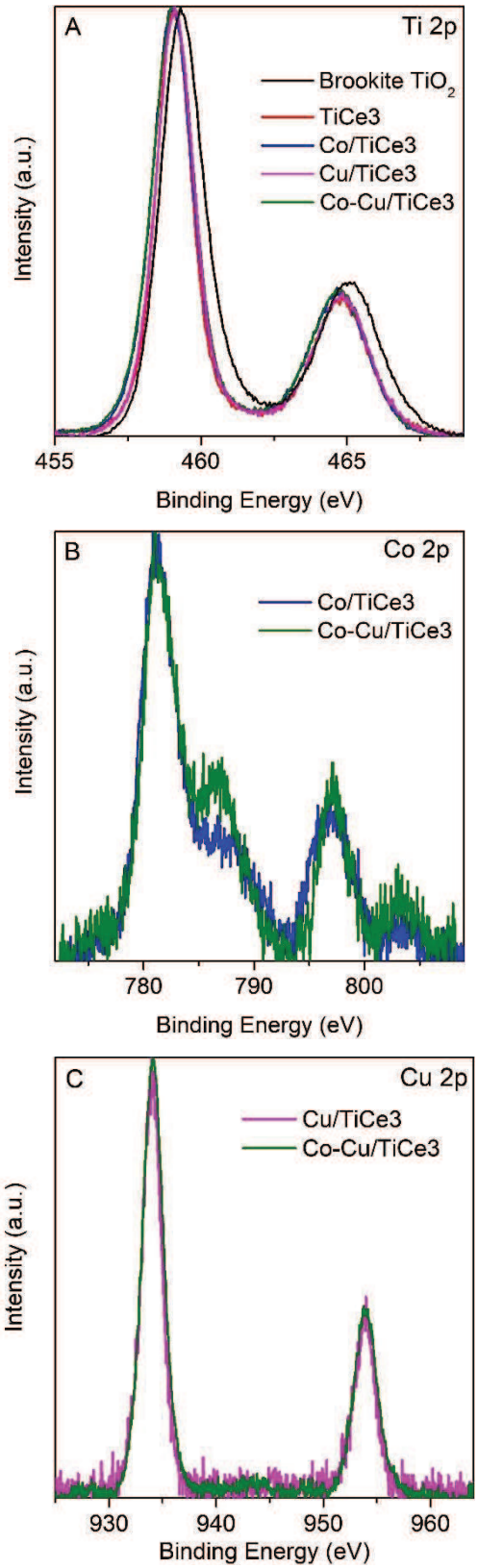
A
Ti 2p
Brookite TiO2
TiCe3
Co/TiCe3
Cu/TiCe3
Co-Cu/TiCe3
Intensity (a.u.)
455
460
465
Binding Energy (eV)
B
Co 2p
Co/TiCe3
Co-Cu/TiCe3
Intensity (a.u.)
780
790
800
Binding Energy (eV)
C
Cu 2p
Cu/TiCe3
Co-Cu/TiCe3
Intensity (a.u.)
930
940
950
960
Binding Energy (eV)

Fig. 5

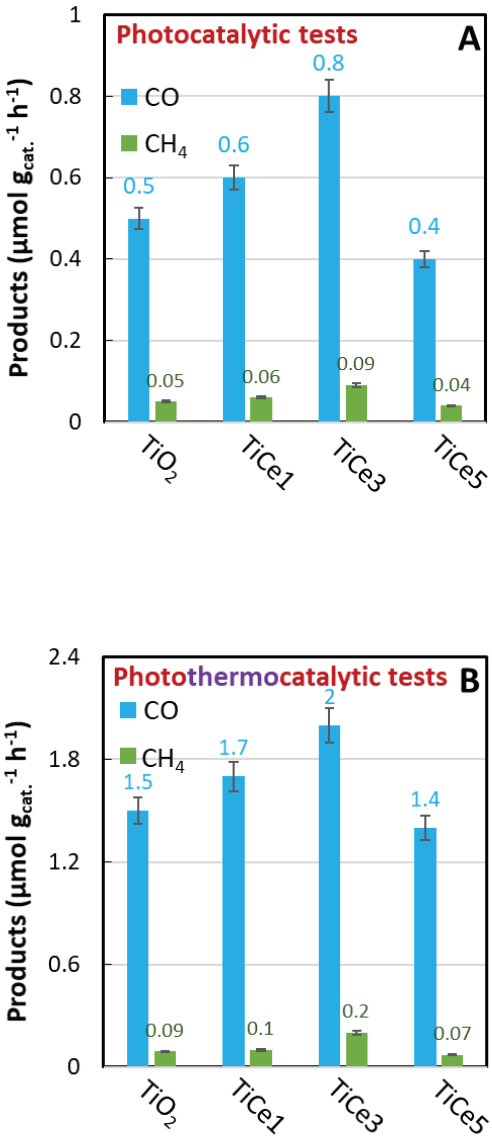
Photocatalytic tests
A
CO
CH4
Products (µmol gcat.-1 h-1)
0.5
0.6
0.8
0.4
0.05
0.06
0.09
0.04
TiO2
TiCe1
TiCe3
TiCe5
Photothermocatalytic tests
B
1.5
1.7
2
1.4
0.09
0.1
0.2
0.07

Fig. 6

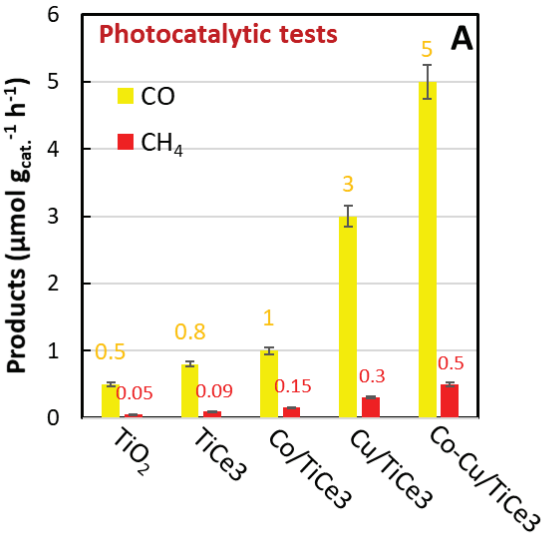
Photocatalytic tests
A
CO
CH4
Products (µmol gcat.-1 h-1)
0
1
2
3
4
5
6
0.5
0.05
0.8
0.09
1
0.15
3
0.3
5
0.5
TiO2
TiCe3
Co/TiCe3
Cu/TiCe3
Co-Cu/TiCe3

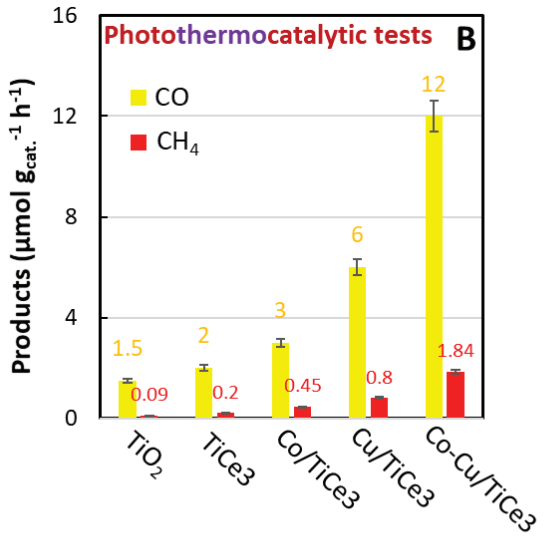
Photothermocatalytic tests
B
CO
CH4
Products (µmol gcat.-1 h-1)
0
4
8
12
16
1.5
0.09
2
0.2
3
0.45
6
0.8
12
1.84
TiO2
TiCe3
Co/TiCe3
Cu/TiCe3
Co-Cu/TiCe3

Fig. 7

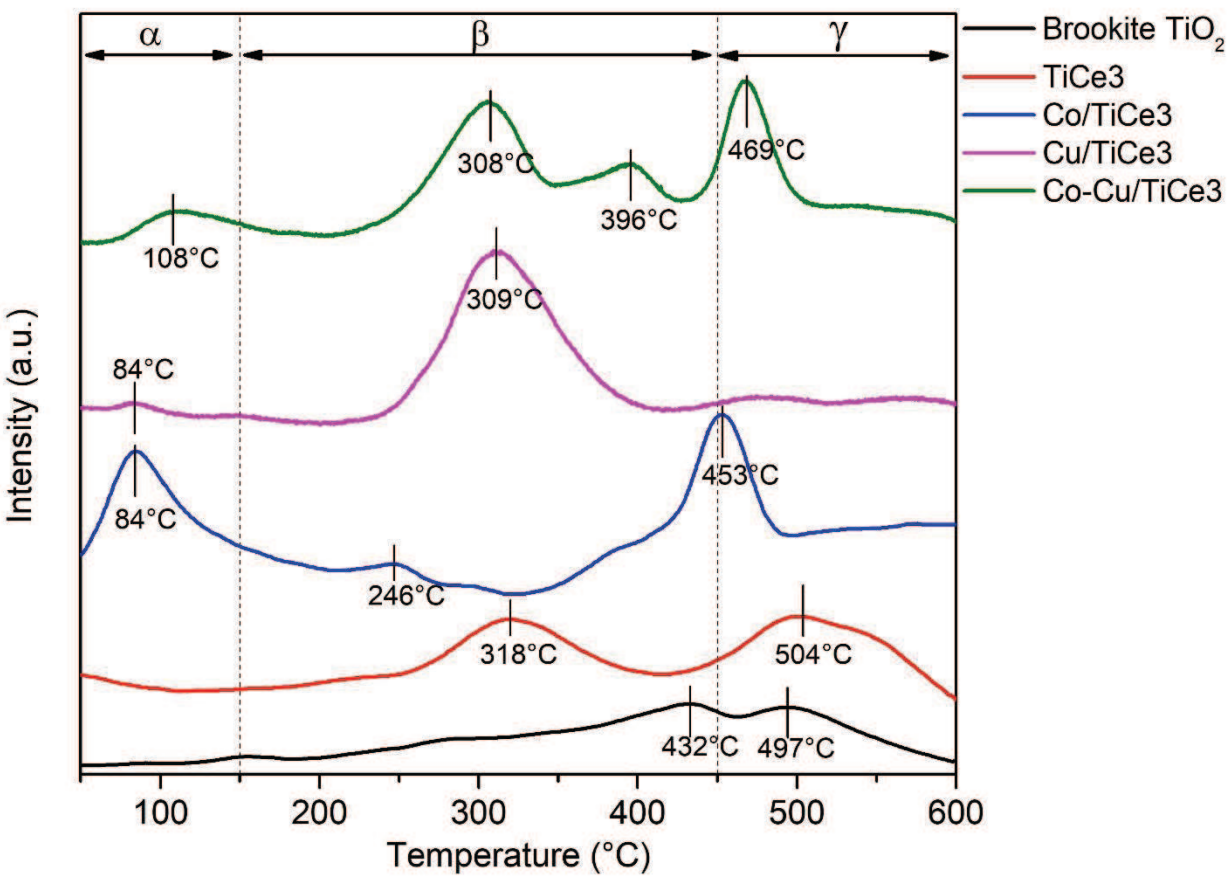
α
β
γ
Brookite TiO2
TiCe3
Co/TiCe3
Cu/TiCe3
Co-Cu/TiCe3
308°C
396°C
469°C
108°C
309°C
84°C
84°C
453°C
246°C
318°C
504°C
432°C
497°C
Intensity (a.u.)
100
200
300
400
500
600
Temperature (°C)

Fig. 8

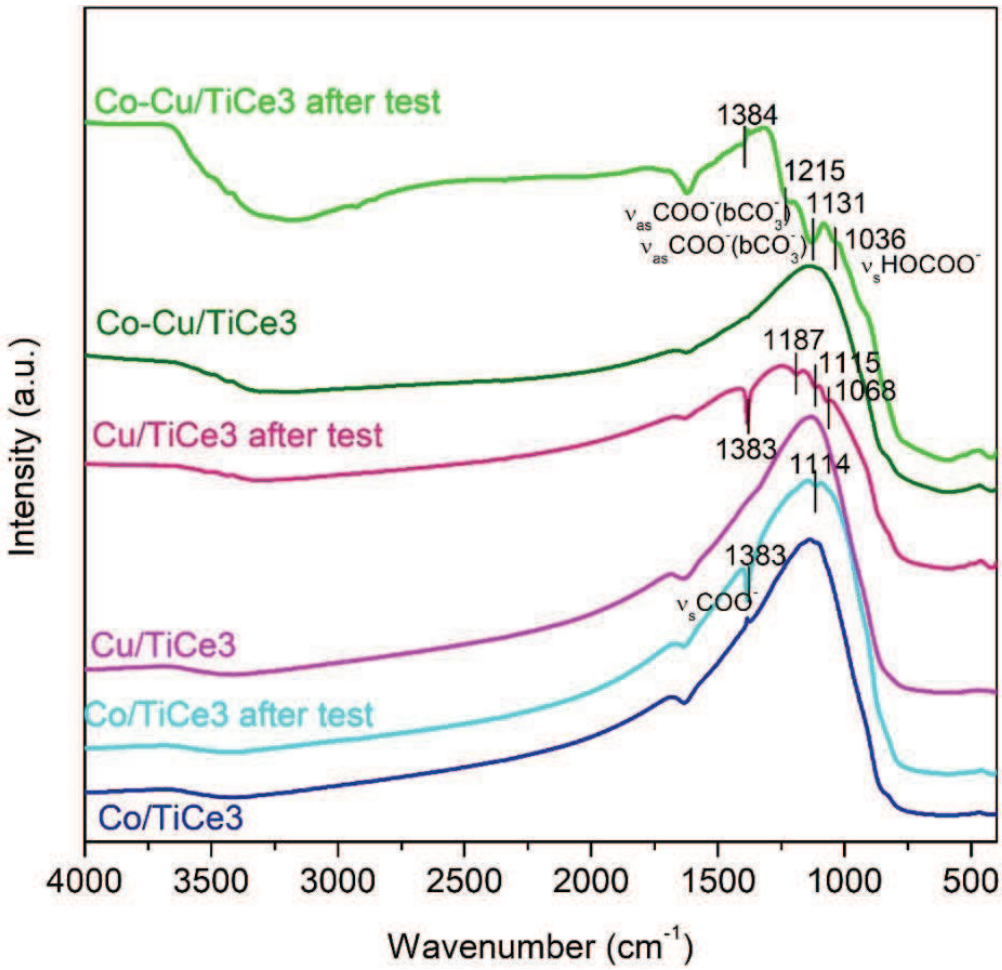
Co-Cu/TiCe3 after test
1384
1215
1131
1036
$\nu_{as}COO^-(bCO_3^-)$
$\nu_{as}COO^-(bCO_3^-)$
$\nu_s HOCOO^-$
Co-Cu/TiCe3
1187
1115
1068
Cu/TiCe3 after test
1383
1114
1383
$\nu_s COO^-$
Cu/TiCe3
Co/TiCe3 after test
Co/TiCe3
Intensity (a.u.)
4000
3500
3000
2500
2000
1500
1000
500
Wavenumber (cm^{-1})

Fig. 9

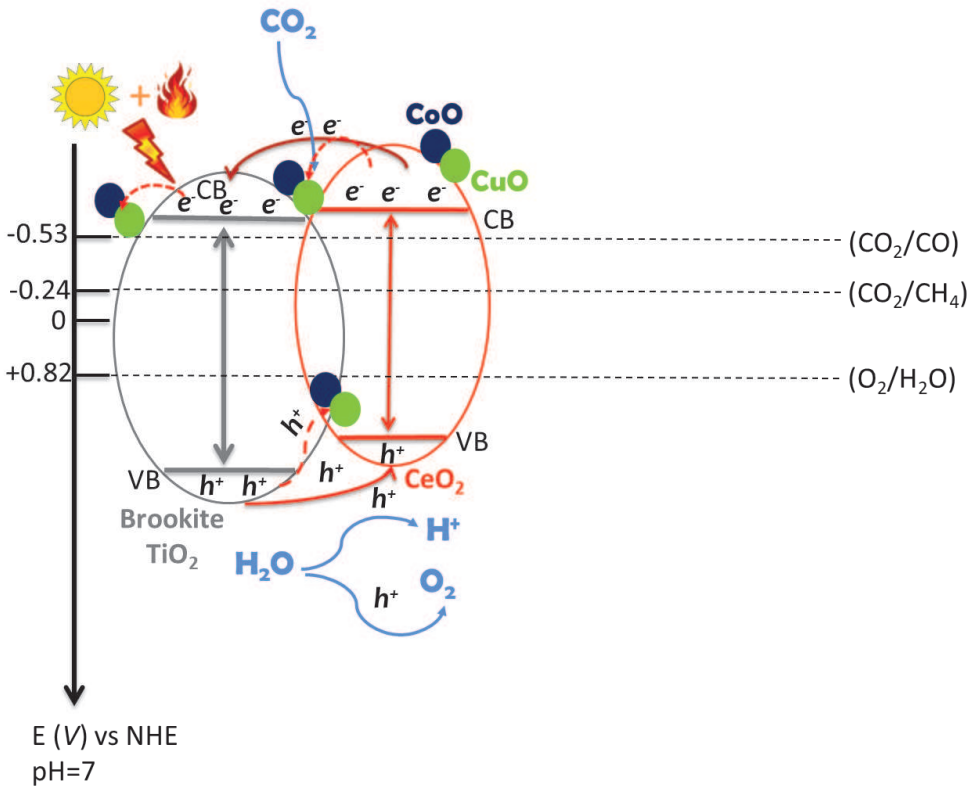
CO2
CoO
CuO
CB
VB
Brookite
TiO2
CeO2
H2O
H+
O2
-0.53
-0.24
0
+0.82
(CO2/CO)
(CO2/CH4)
(O2/H2O)
E (V) vs NHE
pH=7

Fig. 10